Ultramicroscopy 199 (2019) 50–61

Contents lists available at ScienceDirect

Ultramicroscopy

journal homepage: www.elsevier.com/locate/ultramic

Design and simulation of a linear electron cavity for quantum electron microscopy

Marco Turchetti[1,*,a], Chung-Soo Kim[1,a], Richard Hobbs[a], Yujia Yang[a], Pieter Kruit[b], Karl K. Berggren[a]

[a] Research Laboratory of Electronics, Massachusetts Institute of Technology, Cambridge, MA 02139, USA
[b] Department of Imaging Physics, Delft University of Technology, Lorentzweg 1, 2628CJ Delft, Netherlands

ARTICLE INFO

Keywords:
Quantum electron microscopy
Interaction-free measurement
Spherical aberration
Radiation damage

ABSTRACT

Quantum electron microscopy (QEM) is a measurement approach that could reduce sample radiation damage, which represents the main obstacle to sub-nanometer direct imaging of molecules in conventional electron microscopes. This method is based on the exploitation of interaction-free measurements in an electron resonator. In this work, we present the design of a linear resonant electron cavity, which is at the core of QEM. We assess its stability and optical properties during resonance using ray-tracing electron optical simulations. Moreover, we analyze the issue of spherical aberrations inside the cavity and we propose and verify through simulation two possible approaches to the problem. Finally, we discuss some of the important design parameters and constraints, such as conservation of temporal coherence and effect of alignment fields.

1. Introduction

In state-of-the-art electron microscopy, radiation damage due to the minimum electron dose necessary to overcome the source and detector shot noise and resolve sub-nanometer features is recognized as the main resolution limit when imaging biological specimens [1–4]. Williams and Carter refer to this issue as the microscopists' counterpart of the Heisenberg uncertainty principle [5]. Important progress to solve this problem has been made in recent years thanks to the development of cryo-transmission electron microscopy [6,7]. In particular, the coupling of this method with data analysis techniques, consisting of merging data coming from tens of thousands of images, [8] allows reaching sub-nanometer resolution [9]. Even though this technique gets around the radiation-damage problem, it does not allow direct imaging of a single target molecule, which would be the ideal solution. Moreover, even though cryo-TEM shows astonishing results, [10,11] it exhibits some critical issues in terms of effort in preparing several identical samples and complexity of data treatment [8,12]. Alternative techniques are under investigation, such as electron wavefront engineering to verify structural hypotheses [13], entanglement-assisted electron microscopy based on a flux qubit [14], electron holography/ptychography [15,16], multi-pass transmission electron microscopy [17] and quantum electron microscopy (QEM) [18]. This work develops the QEM approach.

A QEM scheme exploits the concept of interaction-free measurement in a resonant electron cavity, that generates and sustains the resonance of two coupled states of the electron wavefunction in order to form images with reduced damage [19]. Several design schemes for a QEM, including new electron optical elements and design considerations, have been proposed in 2016 [18]. These design schemes are based on both linear and circular types of resonators. The cavity of a linear resonator is mainly defined by two electron mirrors. Instead, the form of a circular resonator is similar to the storage ring in particle accelerators [20], and a miniature storage ring has been developed [21]. However, a resonator with controlled electron trajectories for nanoscale imaging applications has not been designed or demonstrated. Thus, before building a physical apparatus, a detailed electron optical design is necessary with consideration of many parameters such as beam diameter, aberration and alignment precision. Particularly important is the validation of the system performance during resonance, which means that a comprehensive study of the electron trajectory evolution with the number of roundtrips is necessary.

To address these issues, in this work we propose a design for a linear resonant electron cavity with two electron mirrors, and we assess its performance through a ray-tracing simulation of the electron trajectories for several consecutive roundtrips. Particularly important in our electron-optical resonant system is the value of electron optical

* Corresponding author.
E-mail address: turchett@mit.edu (M. Turchetti).
[1] These authors contributed equally to this work.

https://doi.org/10.1016/j.ultramic.2019.01.010
Received 23 May 2018; Received in revised form 1 January 2019; Accepted 20 January 2019
Available online 10 February 2019
0304-3991/

properties such as first-order chromatic aberration (C_c) and third-order spherical aberration (C_s), because they build-up at every roundtrip progressively, thus, compromising the resolution. Specifically, we propose two possible modifications to our initial scheme in order to correct C_s that appears to be the dominant aberration in our system. The first one consists of the insertion of a quadrupole-octupole corrector inside the cavity. The second one consists in the substitution of the electron gate mirror with a hyperbolic triode mirror equipped with an Einzel lens to correct the aberrations [22–24]. Finally, we discuss some of the constraints that the peculiarity of our system imposes on the design specifications (*e.g* the path difference between the two coupled beams) and the alignment precision, such as the conservation of the temporal coherence and the parasitic phase error. We also address the necessity of correcting misalignments in the cavity, designing an alignment unit and analyzing the effect of an alignment field on the stability of the system in terms of loss of beam coherence and beam energy spread.

2. Design of the linear resonant electron cavity

In this section, we will explain the working principle of the linear resonant electron cavity, supporting our design with ray-tracing simulation to assess the system performance. Moreover, we will describe the process of geometrical optimization that we used in order to reduce the effect of aberrations.

2.1. Principle of the linear cavity

A QEM consists of an electron gun, illumination optics, resonant cavity, imaging optics, and detectors, as described in [18]. The core of the structure is the cavity, which sustains and controls the electron beam roundtrips. Fig. 1 shows a geometric ray diagram for a linear resonant electron cavity with two electron mirrors, a gated mirror, and a diffractive mirror. The gated and diffractive mirrors are essential components of the resonant cavity that can permit or deny the passage of electrons through their optical axis, therefore controlling the in-coupling into and out-coupling from the resonant cavity. In particular, Fig. 1(a) portrays the schematics of the cavity and its operation in an SEM, while Fig. 1(b) shows the optical diagram of the resonator highlighting the two phases of operation, in-coupling, diffraction, and resonance. The optics of the resonator is designed so that both object and image lie on the same plane, at the mirror surface of the gated mirror side of the resonator. Fig. 1(c) and (d) show the mode of operation of gated and diffractive mirror respectively.

This design is simplified with respect to the one with two electron mirrors and one lens described in [18] in order to reduce the number of alignment units that will be required between every two electron optical elements composing the cavity. Moreover, this scheme is conceived so that the resonator could be placed in a scanning electron microscope (SEM) with a pulsed illumination that can be obtained through laser triggering [25–28] or using a fast blanker [29,30]. A comparison between the two methods has also been proposed in [31]. The SEM column, consisting of the electron gun and focusing optics, is used to produce a focused electron beam. In the following, we analyse the different phases of operation.

2.1.1. In-coupling

The gated mirror (also referred to as the 'barn door' in [18]) controls the access of this beam to the resonator. A similar concept was proposed for in-line aberration correction in [32]. This electron optical element is comprised of six stacked electrodes placed at the top of the

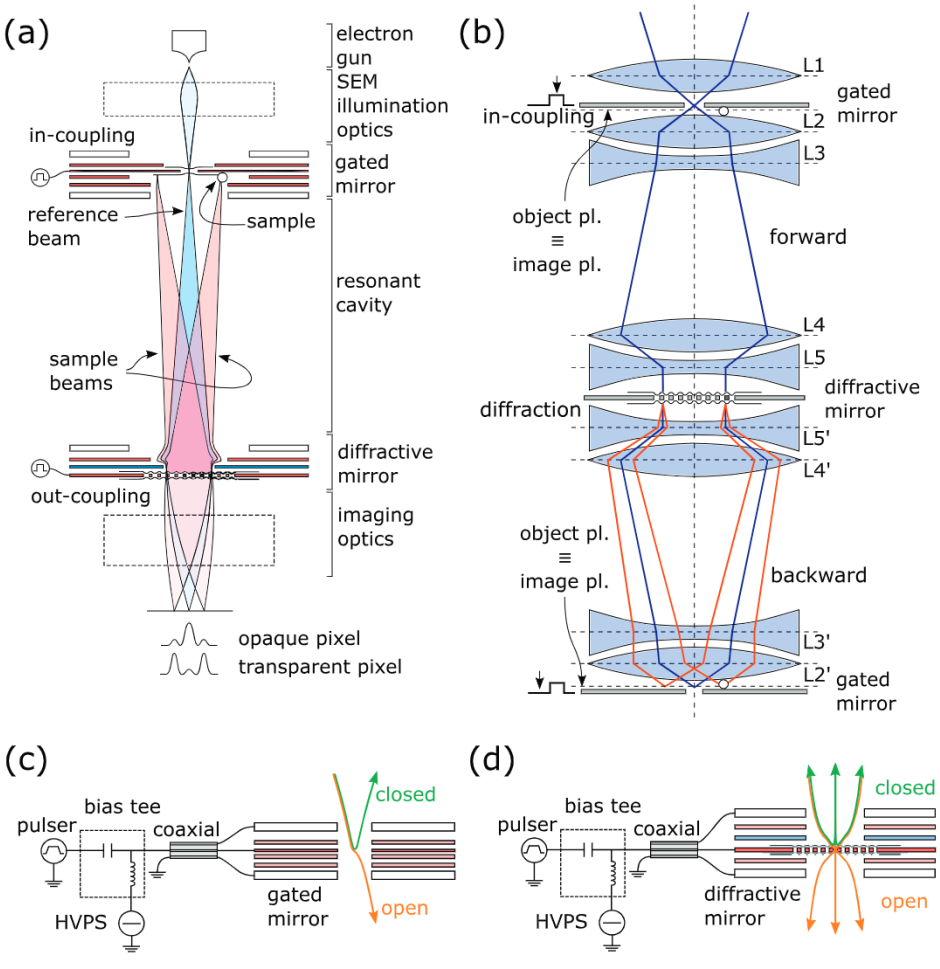

Fig. 1. Schematic (a) and optical diagram (b) of the linear resonant cavity, with highlight on the operational principle of the two main elements: the gated mirror (c) and the diffractive mirror (d). The electron gate controls the access of the electrons inside the cavity while the diffractive mirror acts as a two-state coupler. In (c,d) the closed and open mode of operation of these elements are portrayed highlighting the corresponding electron trajectories in green and orange respectively. Such a cavity sustains the resonance of both the reference and the sample beams (in blue and red in the picture), which are the two states of the electron wavefunction generated by the mirror. The object is placed in the sample-beam path. According to interaction-free measurement theory, in the case of a transparent sample pixel, during the resonance, the beam intensity is gradually transferred to the sample beam. On the contrary, in the case of an opaque pixel sample, most of the intensity remains in the reference beam. The beam is then outcoupled, and its intensity is recorded on a phosphor screen. The two phases of in-coupling and resonance are highlighted in separate mirrored diagrams in (b) for clarity. In this diagram, the positions of the object and image plane as well as the lenses Li (where i denotes the lens number) that compose the gated and diffractive mirrors are highlighted. The same lenses are denoted as Li' in the resonance part of the diagram. (For interpretation of the references to colour in this figure legend, the reader is referred to the web version of this article.)

resonator. The potential at the gated mirror is usually tuned so that it acts as a double-sided mirror. In this condition, the electrons external to the cavity cannot enter the cavity, while the resonance stability is maintained internally. To let the electron access the resonator, a positive pulse is applied to temporarily lower the central electrode's negative potential and open the gate.

2.1.2. Resonance

Once the beam enters the cavity, it reaches the diffractive mirror. This is a four-electrode element. Here, the electron wavefunction is split into two components by the interaction with a potential grating generated by the periodic pattern of the mirror's lowest electrode. This diffraction scheme is similar to the one in low energy electron diffraction (LEED) [33]. However, the use of a potential surface for the diffraction in place of a physical surface ensures the absence of direct interaction with the physical grating, which prevents intensity loss by inelastic scattering as can happen in LEED [34]. The zeroeth diffraction order, that will be referred to as the "reference beam", is reflected on the same path of the incoming beam. The first order diffracted beams generated by the grating instead will be referred to as the "sample beam". The diffractive electron mirror also generates higher order diffracted beams. The intensities of these orders depend on the amplitude of the sinusoidal surface at which the electron are reflected. Hence, if the diffractive mirror potential is tuned correctly, the loss to the higher order can be made negligible. Moreover, as described by Yang et al. [35] these higher-order beams can be blocked by a beam limiting aperture. This approach can effectively preserve two beam intensities by using the quantum Zeno effect. Therefore, if necessary, an aperture can be added at the gated mirror. Note that we cannot block one of the first order diffracted beams since in this set-up the intensity in the $+1$ beam appears in the -1 beam after the next round in the resonator.

The cavity design permits resonance of both the reference and sample beams, which are coupled by diffraction at the potential grating. To reduce the complexity of the "electron diffraction on a potential grating" problem treatment (yet to be experimentally demonstrated), the cavity is designed so that the reference beam reaches the potential grating parallel to the optical axis. The fundamental condition is that the electric field at the grating has to be high enough so as to reduce the effect of the energy distribution of reflecting electrons. In fact, assuming the electron beam has an energy spread $\Delta E = 0.7$ eV, [5] the electrons with higher and lower energies with respect to the average are reflected at different potential surfaces, and the distance of such surfaces from the ideal surface is lower with a higher electric field. In this particular case, with an 8 kV/mm and a 16 kV/mm electric fields $\mathcal{E}$ we would have a longitudinal spread of the mirror surface location $\Delta x = \Delta E/q\mathcal{E}$ of 87.5 nm and 43.75 nm, respectively. Moreover, a higher electric field at the mirror guarantees a higher amplitude of the periodic potential at the reflection surface for the same mirror electrode potential.

The present set-up is meant for proof-of principle experiments, so we may choose the sample as we wish. We plan to place the sample on a thin conductive foil electrode with a center hole for the reference beam. For the first experiment, the sample is going to be a symmetric pattern of holes on the foil itself, where the sample beams can be either blocked or transmitted. This foil is to be positioned on an equipotential plane close to the mirror surface, where the electrons still have a few electronvolts energy. The voltage on this electrode should be such that the electric field at both sides of the foil is equal, thus avoiding a lens effect of the holes. We expect that the resonance function will not be not disturbed. It is worth noticing that the foil is going to act as the blocking aperture for the higher order beams, therefore confining the intensity to reference and sample beams.

In this work we assume a binary amplitude object model, that is to say that different regions of the sample can be either opaque or transparent. Such an object allows us to apply straightforward interaction-free measurement theory. A real sample with different levels of transparency can be imaged as well in this system as demonstrated by Thomas et al. in [36], but the treatment of the problem is more complex. However, for a proof of concept of the measurement scheme a binary object would suffice. According to interaction-free measurement theory, in the case of a transparent sample pixel, during the resonance, the beam intensity is gradually transferred to the sample beam. On the contrary in the case of an opaque sample pixel, most of the intensity remains confined in the reference beam [18,19,37,38].

This system sustains the resonance for a unique reference state, so the sample cannot be scanned by moving the beam. Therefore it has to be imaged by moving the sample itself with a nano-stage controlled by a piezo-motor. We recognize that having to move the sample is a limitation of our current design because it will be challenging from a mechanical standpoint to move a sample in such a small region and because in the long run it could represent a bottleneck for the system resolution. Therefore, future designs will have to address this issue and some better solution will have to be implemented. However, for a proof-of-concept demonstration of the technique it is a suitable solution.

2.1.3. Out-coupling

After a sufficient number of roundtrips, a pulse is applied to increase the diffractive electron mirror potential, letting the beams out of the resonator. The necessary number of roundtrips can be estimated considering the expected probability of amplitude transfer of the wavefunction that allows discriminating between an opaque and a transparent pixel [38]. In order to allow the out-coupling of the electrons the grating has to be a transmission free-standing grating, similarly to the grating used by McMorran et al. in [39]. The out-coupling process is summarized in Fig. 1d. After the signal is out-coupled increasing the negative diffractive mirror potential using a voltage pulse, the beams pass through a lens which focuses them on the detection plane and the outcome of the measurement is recorded on a single electron sensitive camera such as the Gatan K3 IS. The out-coupling is the only step of the measurement in which the beam can interact with the grating. Since the out-coupled intensity can vary depending on whether the constructive interference fringes line up with the grating bars or not, in order to maximize the out-coupled intensity it would be beneficial to use a low duty-cycle grating and maintain during the out-coupling process a non-zero voltage on the grating to produce a stronger phase grating effect.[2] It is also worth noting that in the future other out-coupling and detection schemes can be investigated. One possibility would be to use the grating itself as a spatial filter during the out-coupling and then with a single monolithic detector relate the out-coupled intensity to the specimen-induced phase [40].

2.2. Design constraints

We aim to integrate the electron cavity design presented in this paper into a conventional SEM. We have considered a field emission SEM, LEO 1525 (ZEISS) for our design, but most conventional SEMs could potentially be used. We need to consider the following practical points:

1 The length of electron cavity is limited to around 120 mm for the resonator to fit in the SEM chamber. This length still requires a significant modification of the stage. Most conventional SEMs can deal with such modification of the stage and the SEM chamber can deal with 120 mm-long electron column. The required stage should handle the heavy weight of the electron cavity and also have a through-hole along the SEM colomn optical axis for beam out-coupling.
2 The length of the cavity should also consider the roundtrip time

[2] We thank the reviewer for pointing this out.

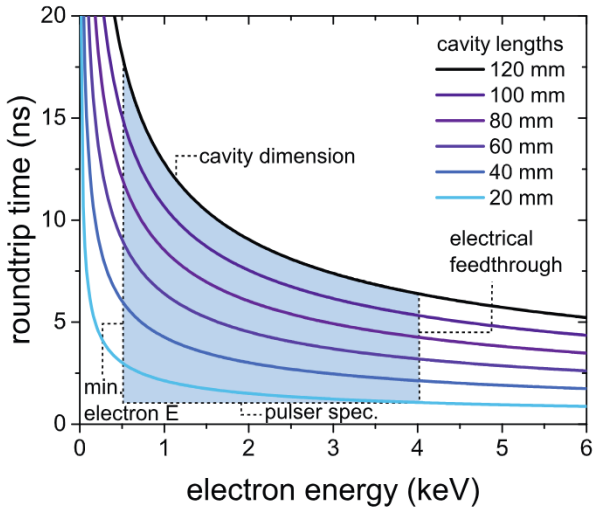

Fig. 2. The dependence of the round-trip time on electron energy for different cavity lengths. We highlighted on the graph a parametric window in which to design the resonator by considering the physical dimensions of microscope chamber and other experimental limits such as the pulse-generator specification, the maximum voltage allowed by electrical feedthroughs and the minimum electron energy available in the SEM.

(which is related to the energy of electron) and the correspondent limitation on the pulse length, that, once electrons are allowed into the cavity, has to close the gated mirror before they complete a roundtrip. Therefore, we are limiting the roundtrip time to 1 ns as building a sub-nanosecond high voltage pulse generator can be challenging.

3 High speed and high voltage electrical feedthrough is only commercially available up to 4 kV.

4 The beam separation between reference and sample beam as functions of energy of electron, grating pitch, and the length of resonator;

5 The lowest energy that we can use in our SEM is 500 eV.

Fig. 2 shows the roundtrip time with the electron energy for different cavity dimensions, indicating a possible operational window by taking into account some of the constraints previously explained. The selected parameters for design and simulation are 3 keV of electron energy and 60 mm of cavity length.

2.3. Design of optic components

2.3.1. Gated mirror

Fig. 3 shows electrodes' geometries and analysis of the gated mirror. The electron-optical simulation described in this paper are performed using Lorentz-2D-E and Lorentz-3D-E software from Integrated Engineering Software Inc, and employing boundary element method for the calculation of the potential distribution. Fig. 3(a) illustrates the structure of the gated mirror and equipotential lines. This element is comprised of six stacked electrodes. The M3 electrode is the core of the electron gate because it hosts the signal that opens and closes the electron path. V_{M1} and V_{M6} are ground potentials and their function is to insulate the unit and guarantee that the electrons do not experience a modification of their kinetic energy after passing through the structure. V_{M2} and V_{M4} are responsible for the in-coupling and the reflection plane modulation. Instead, V_{M5} is used to adjust the stability of the sample beam trajectory depending on its diffraction angle. Such a feature will be discussed in more detail in the next section. It is worth noting that the latter potential has almost no influence on the position of the Gaussian mirror plane, thanks to the fact that this surface lies within the lens form, therefore the sample beam resonance condition can be achieved practically independently from the other electrodes' configuration. Fig. 3(b) portrays the axial potential distribution of the gated mirror in the two different configurations, open and closed, that corresponds to in-coupling and resonance, respectively. The gated mirror switching time has to be lower than the time necessary for an electron to complete a full roundtrip. For a 60 mm cavity with 3 keV electrons, the roundtrip time is around 4 ns, as can be seen in Fig. 2. In Fig. 3(c) and (d), we plot the radial potential lines of the mirror plane as a function of applied potentials with a fixed bore diameter (c) and different bore diameters with a fixed applied potential (d). This plane is the azimuthal plane that on the optical axis has a value of −3000 V, and in an ideal situation should exhibit a constant value throughout the entire plane. A non-uniform potential means that the mirror surface is not flat. In Fig. 3(c), this graph is portrayed for different values of the potential and it shows that a higher potential corresponds to a flatter condition of the mirror surface. However, a higher potential corresponds to a higher amplitude of the pulse necessary to operate the gate. Achieving a high amplitude for a few nanosecond pulse width would increase the feedthrough technical design complexity and would require a customized pulse generator. Thus, a lower amplitude is preferable. Fortunately, as shown in Fig. 3(d), we can also achieve a flat potential with the same pulse by decreasing the diameter of the M3 aperture. Specifically, we designed this electrode with a central aperture of 20 μm in diameter, which is quite small with respect to conventional lens bores, that are usually of the order of millimeters. In this way, we can employ a relatively small pulse (V_P = 100 V) to switch between open and closed configuration. This condition is more suitable for a commercially available high-frequency pulse generator.

2.3.2. Diffractive mirror

Fig. 4 illustrates the design of the diffractive tetrode mirror. This element is composed of four electrodes, all cylindrically shaped. This type of tetrode mirror is known to be able to control the back focal length, analogously to cathode objective lens or emission lens [42]. The lower electrode here is modeled as a flat surface, as we are simulating electron trajectories without considering the electron phase that would cause diffraction. In the real case, this electrode will be shaped as a grating that generates the periodic surface potential responsible for the diffraction that causes splitting and coherent coupling between the sample and the reference beams. The two lowermost electrodes at V_{N1} and V_{N2} create a negative cathode lens. In particular, the negative potential V_{N1} has to be maintained higher than the corresponding electron energy of 3 keV to obtain a mirroring effect.

In order to achieve the desired diffraction, it is necessary that the reference beam reaches the grating with a perpendicular trajectory and that the zero energy periodic surface be at the correct distance from the physical grating so that such a surface exhibits an acceptable spatial amplitude to generate diffraction. In particular, such sinusoidal amplitude modulation determines the beam splitting intensity between diffraction orders. In order to predict the necessary amplitude modulation it is necessary to solve the Shroedinger equation for the electron wavefunction all the way from the field free region. This is necessary as the electron is not only diffracted at the classical turning point (the modulated mirror potential) but already feels the modulation both on its incident and reflected path. Thus, it experiences much more modulation (i.e. path length difference) than just these few angstrom. A complete numerical model of this problem has been proposed in [41]. The result of this study show that a typical spatial amplitude to get a beam splitting of few percentages in the first order (sample) and the rest in the zeroth order (reference) is expected to be of the order of angstroms.

V_{N2} is kept to a potential that fixes the electric field to 16 kV/mm. Such high electric field is necessary to reduce the energy spread effect of the incoming electron beam. V_{N3} instead is used to control the focal position of the mirror. Finally, the upper electrode is grounded so that the unit is isolated from the rest of the elements creating a zero field

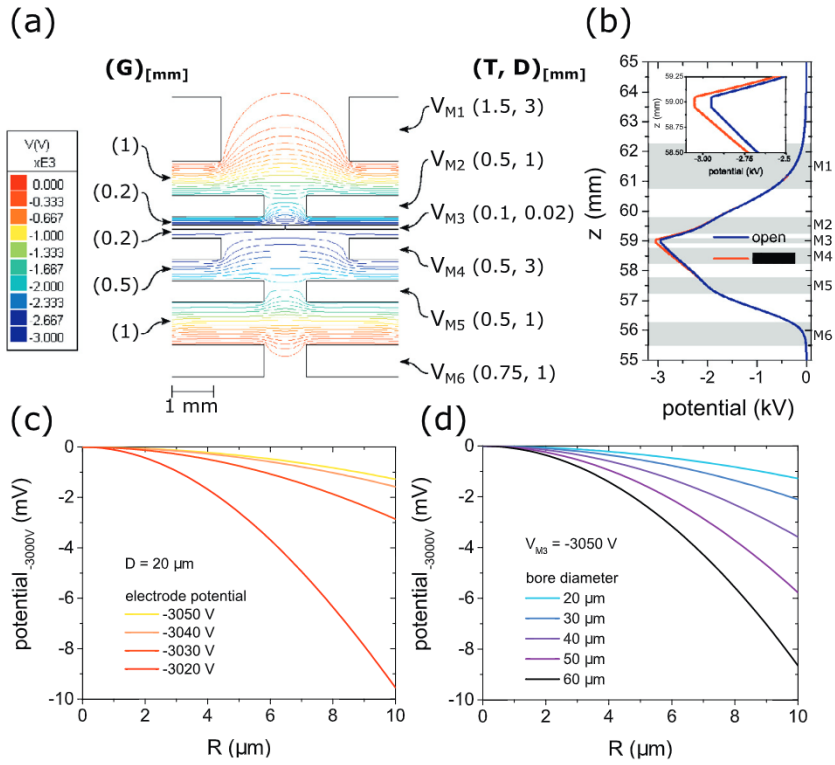

Fig. 3. (a) Geometry and potential distribution of the electron gated mirror. The multi-colored lines indicate equipotential surfaces. The potential used for the simulation are the following: $V_{M1} = V_{M6} = 0$ V, $V_{M2} = -2000$ V, $V_{M3} = -3050$ V, $V_{M4} = -2990$ V, $V_{M5} = -2080$ V. Also listed are the geometrical parameters: gap G to the left, thickness T and bore diameter D to the right. (b) Axial potential at the electron gate in open and closed configuration. The position of the electrodes is also indicated on the graph by the gray rectangles. (c) Dependence of the ideal mirror surface potential with the radial distance from the optical axis, for different values of the M3 electrode potential. (d) Dependence of the ideal mirror surface potential with the radial distance from the optical axis, for different values of M3 aperture diameter. Comparisons of (c) and (d) provide a means of design trade-off between electrode potential and bore diameter.

region inside the cavity.

2.4. Ray tracing of electron resonator

The following simulations are performed using LorentzEM software from IES. The initial condition for the electron trajectory simulation in resonance is achieved by emitting electrons close to the mirror electrode, specifically at the mirror surface (− 3000 V). The reference beam electrons are emitted with zero energy so that they are accelerated perpendicular to the mirror surface. Despite the fact that a full solution of the Shroedinger equation for the electron wavefunction from the field free region to the modulated potential region is necessary to capture the exact behaviour of the electron beam, to predict the electron trajectory after diffraction we can use a momentum kick approximation. In order to simulate the momentum kick due to the grating $p = h/d$ (with d pitch of the grating), the electrons composing the sample beam are emitted with in-plane energy parallel to the mirror surface of $E = h^2/2md^2$.

Fig. 5(a) shows the result of the electron beam in-coupling simulation, that is to say, the ray-tracing of the 3 keV electron trajectories when the gated mirror is open and the electrons are free to enter in the resonator. In order to open the gate, a 100 V pulse is applied to the central electrode bringing V_{M3} potential from -3,050 V (closed configuration) to -2,950 V (open configuration). Once the pulse effect is concluded the gate is closed, and the electron resonates inside the cavity. This situation is portrayed in Fig. 5(b), which shows the simulation of the marginal and axial rays (i.e. the most external ray of the beam and the central one, respectively) of both the sample and the reference beam. In this simulation, the two beams successfully perform 5 roundtrips, demonstrating the correct functioning of the resonant cavity built as a result of the integration of the two units. Fig. 5(c) shows a close-up of the reference beam marginal ray trajectory, which allow us to distinguish the different round-trip trajectories and visualize the system sustainability of the resonance for $N = 5$. In this context, we can define the trace stability as the difference between the electron trajectories of two consecutive round-trips, calculated at the mirror

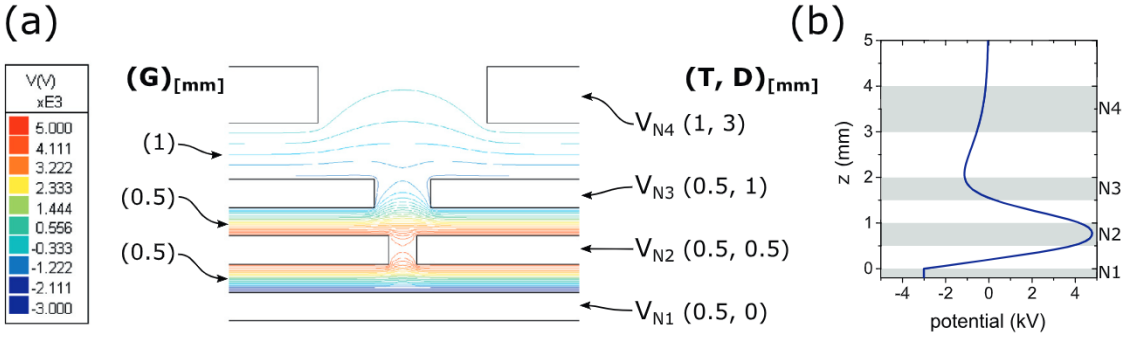

Fig. 4. (a) Geometry and potential distribution of the tetrode electron mirror. The potentials used for the simulation are the following: $V_{N1} = -3010$ V, $V_{N2} = 5000$ V, $V_{N3} = -1467$ V, $V_{N4} = 0$ V. This configuration generates a 16 kV/mm electric field between the two lowest electrodes. In the picture are also listed the geometrical parameters: gap G to the left, thickness T and bore diameter D to the right. (b) Axial potential at the diffractive mirror, where z is the distance from the mirror electrode.

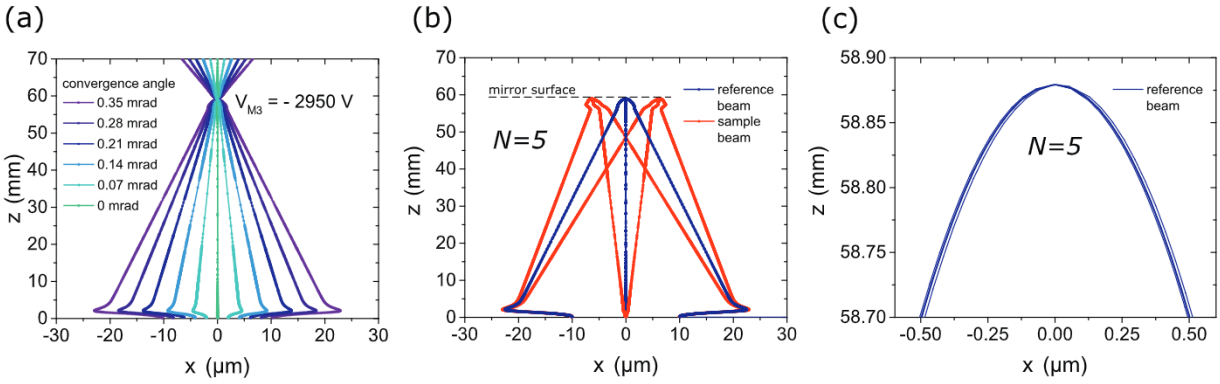

Fig. 5. (a) Trajectory simulation of the in-coupling. Different colors indicate different beam-convergence angles. (b) Ray-tracing simulation of the marginal and paraxial rays of both reference and sample beams in resonance configuration, for $N = 5$ roundtrips. The simulation was performed emitting the electrons starting on the mirror surface (the -3000 V surface) with a direction perpendicular to that surface for the reference beam and imposing a lateral momentum kick, as explained in the main text, to generate the sample beam. (c) Close-up of the electron trajectory of the reference-beam marginal ray near the mirror surface at the gated mirror. The close proximity of adjacent trajectories demonstrates the cavity stability.

surface of the diffractive mirror. This criterion is important because the grating mirror is acting as a two-state coupler between sample and reference beam. Hence, the position of the beam on the grating mirror gives us an indication of the quality of the measurement in term of its compliance with the IFM criteria. In fact, if the stability were to be worse than the grating period, no build-up of the signal in the sample beam due to consecutive interference phenomena could occur. From the simulation result, we obtain a marginal ray trace stability below 1 nm, which results in a final spread of the trajectories at the diffractive mirror of about 2 nm. This result validates our design in term of stability, providing a constraint to the achievable resolution of the order of few nm. We can conclude from this simulation that stability is not going to be the limiting factor to the achievable resolution. The limiting factor is going to be instead spherical aberration that entails the paraxial rays (i.e. the rays closer to the axis) having a different focal position with respect to the marginal rays. This issue is going to be addressed extensively in the next section.

In this simulation the sample beam is generated by initializing the beam with an energy parallel to the grating surface of $E = 10$ meV, which corresponds to a grating with a ~ 12 nm pitch. This small pitch is used here in order to better visualize the separation between reference and sample beams (smaller pitch corresponds to higher diffraction angle, hence higher separation). In the actual system, a larger pitch would be preferable because it would be easier to fabricate, and it would entail a lower intensity loss during out-coupling. Our design can be adapted for different pitches. Fig. 6 shows how V_{M5} can be used to tune the angle of the sample beam whose resonance is sustained by the cavity. This angle depends on the periodicity of the grating following the equation $d \sin\theta = m\lambda$, where d is the grating pitch, λ is the electron wavelength, θ is the diffraction angle and m is the diffraction order, which in our case is ± 1 as we are interested only in the first order. This tunability is important because it allows us to use different pitches in the same system. Also, the machining of the resonator will not be perfect; therefore, having this additional degree of freedom gives us room to correct for such non-idealities.

2.5. Optimization of diffractive electron mirror

One of the main problems of the resonant cavity (as described so far) is that the tetrode mirror is composed of a cathode lens, which is an element strongly affected by aberrations, with C_c and C_s that scale with the fourth and second power of the magnification, respectively [43–45]. This is a well-known problem in low energy electron microscopes (LEEM), which also employ cathode lenses [46]. This effect in our case is amplified by the fact that the electron beam resonates inside the cavity. Therefore, these deviations from ideal behavior worsen with

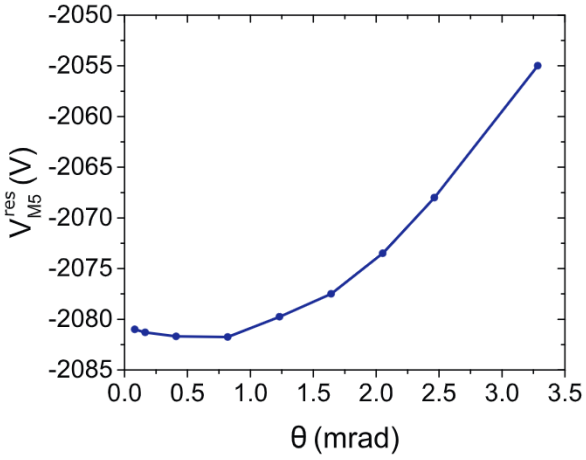

Fig. 6. Dependence of the V_{M5}^{res} on the diffraction angle θ. V_{M5}^{res} is the potential of the electrode M5 that guarantees the resonance of the sample beam. The angle θ instead is imposed by the grating periodicity. Therefore, the voltage can be easily tuned to adapt the setup to different gratings and to compensate for non-idealities in the grating periodicity.

the number of roundtrips and the beam size increases progressively, as can be seen in Fig. 7(d), causing a degradation of resolution. A standard cathode objective lens (contrary of a standard einzel lens) can be corrected for aberrations by modifying the cathode electrode geometry so as to induce hyperbolically shaped potentials that would correct the aberrated electron wavefront [22,47]. However, this correction scheme cannot be easily applied to our cathode lens, because such component also hosts the diffraction grating that has to generate the sample beam and couple it to the reference beam. This task would be very challenging if bending or any other variation of the grating geometry were introduced for aberration correction. A different design, employing a transmission coupler in place of a reflective one, would not have this problem, but it would have to deal with a loss of intensity due to inelastic scattering, *e.g*, volume plasmon and thermal diffuse scattering. Therefore, alternative strategies have to be found in order to overcome the aberration build-up. The value of spherical and chromatic aberration of our tetrode mirror base geometry are $C_{sN} = 18 \cdot 10^3$ m and $C_{cN} = 2.97$ m, respectively. These coefficients are obtained by performing a simulation using LorentzEM software. Analogously, the aberration coefficients of the gated mirror are $C_{sM} = 4.28$ m and $C_{cM} = 0.052$ m. In the following, we will address the issue of C_s because in our case it is the predominant aberration. Moreover, in principle, the effect of C_c could be reduced by improving the electron source energy spread, i.e.,

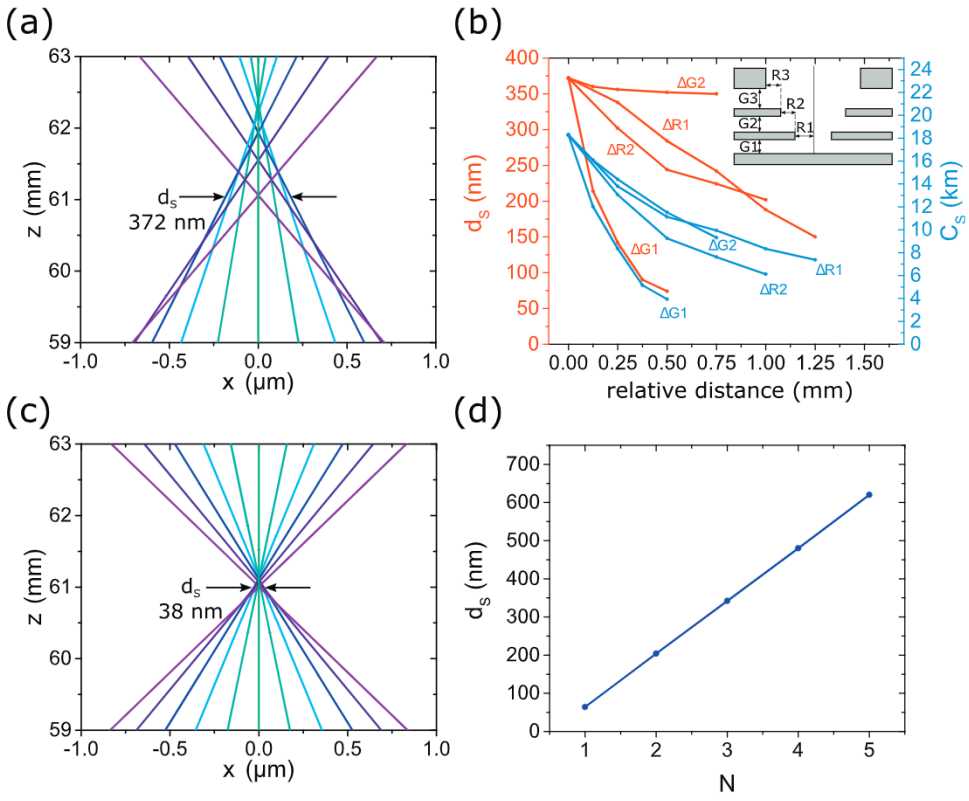

Fig. 7. (a) Trajectory simulation of the beam reflected up from the tetrode mirror showing the effect of spherical aberration before the geometrical optimization. (b) Influence of geometrical parameters $G1$, $R1$, $G2$, $R2$ on the total mirror lens aspherical aberration coefficient C_s and on the spot size d_s at the gated mirror, which is directly related to the spherical aberrations. In particular, the simulation is performed at the back focal plane at the gated mirror, maintaining a 16 kV/mm electric field on the mirror electrode. The initial values of these parameters are $G1 = G2 = 0.5$ mm, $R1 = R2 = 0.25$ mm, $G3 = R3 = 1$mm. (c) Trajectory simulation of the beam coming from the tetrode mirror showing the effect of spherical aberration after the geometrical optimization. (d) Results of a full cavity simulation showing the dependence of the spot size d_s at the gated mirror as a function of the number of roundtrips.

placing an energy filter at the top of the gated mirror. However, future work should tackle also the influence of C_c. We also consider mainly the aberrations due to the diffractive mirror, since its contribution is the greatest.

Fig. 7(a) illustrates the effect of C_s due to the tetrode mirror on the electron trajectories, in particular, on the spot size d_s, using our base configuration for the mirror, shown in Fig. 4(a). The first step to minimize aberrations is to optimize the mirror geometry. Fig. 7(b) portrays the influence of the geometrical parameters on the spot size d_s and the correspondent value of C_s. These results are extracted from the electron optical simulation imposing the electrode potentials so as to satisfy two conditions: the position of the back-focal plane being fixed at a distance corresponding to the position of the gated mirror, and the electric field between the two lowermost electrodes being maintained at 16 kV/mm. The fact that a flat potential at the grating electrode is required for diffraction limits the maximum radius R1 of the anode electrode, which influences the aberration of the tetrode electron mirror.

Fig. 7(c) shows the result of the optimization through ray-tracing simulation. Perhaps it is possible to reduce the aberrations to zero as in the design of Van Aken et al. [48], but we have not yet found such a configuration in combination with a high field strength on the grating mirror. As can be seen from the picture, after the optimization, the spot size is reduced from 372 nm to 38 nm, thus improving the resolution by a factor of 10. This spot size is close to the diffraction limited spot size for the considered semiangle and acceleration voltage $d_d = \frac{0.753}{\alpha\sqrt{V}} \sim 40$ nm. However, as can be seen in the simulation portrayed in Fig. 7(d), d_s grows linearly with the number of roundtrips N. Moreover, having lower spherical aberrations would be beneficial when the system is operated with higher semiangle and hence smaller d_d. Typical SEMs can operate with a resolution of few nanometers for an energy of 3 keV. Therefore, this limit to the resolution remains non-negligible. This spot size may allow us to demonstrate a proof-of-concept experiment of an electron cavity for QEM. However, in the future, a further correction would be necessary for the ultimate application of imaging biomolecules. To address this issue, we propose some strategies for further improving spot size/resolution in the following section. In wave optics, spherical aberration is a phase change proportional to the fourth order of the distance to the optical axis. One may wonder if this will affect the action of the grating. However, we expect this not to be the case since the reference beam and the sample beam are almost overlapping, so the relative phase change will be small.

3. Aberration correction in a linear resonant electron cavity

In this section, we propose and simulate two improved designs for the linear resonant cavity that allow correcting C_s generated by the tetrode mirror.

In 1936 Otto Scherzer demonstrated that spherical and chromatic aberration, regardless of the fabrication precision, cannot be eliminated by improving the quality of the lenses and that for an electrostatic round lens the aberrations do not change sign (Scherzer's Theorem) [49]. As we established in the previous section, our geometrical optimization is not conclusive, and we need to induce an opposite sign of aberration. This can be done through one of the following means:

1 Breaking the rotational symmetry exploiting multipoles fields [50,51]
2 Introducing orthogonal symmetries using elements such as mirrors [22,47]
3 Using time-varying potential with pulsed beam [52]
4 Introducing space charges on the electron optical axis placing a conducting foil or a mesh in the beam path [53]

The third method had not been demonstrated, and the fourth method induces inelastic scattering, resulting in the loss of intensity. Thus, these two methods are not considered in our work. In the following, we are going to apply the first and the second methods to our system and highlight their different characteristics.

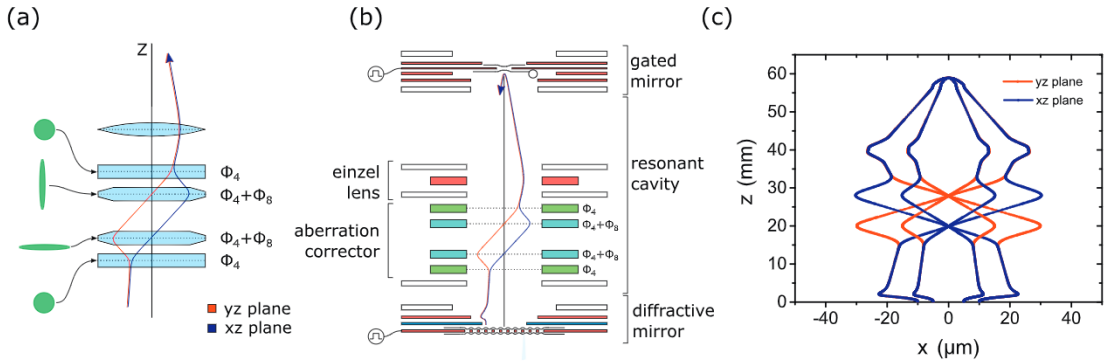

Fig. 8. (a) Optical diagram of the quadrupole-octupole corrector employed in our design. The corrector consists of 4 multipole elements, on which a superposition of quadrupole and octupole fields is applied to correct the aberration. The blue rectangular symbols define the quadrupoles, and the blue octagonal symbols define the octupole elements. The beam shape at the lens planes is represented in green. (b) Schematics of the cavity corrected for spherical aberrations introducing the quadrupole-octupole corrector. (c) Raytracing simulation portraying both the marginal and a paraxial ray of the same cavity. (For interpretation of the references to colour in this figure legend, the reader is referred to the web version of this article.)

3.1. Quadrupole-octupole corrector

The first approach that we are going to discuss is shown in Fig. 8(a) and (b), and consists of the insertion of a quadrupole-octupole corrector in the cavity. The corrector comprises four multipole elements plus two external grounded electrodes to insulate the structure. An einzel lens is also placed above the corrector to restore the focusing of the beam after its transit through the system. This design is based on the superposition of quadrupole and octupole fields on the four multipole units [54]. The optical diagram and the working principle of the system are illustrated in Fig. 8(a). This system exploits quadrupole field two-fold astigmatism to force the beam into a stretched elliptical shape in the two azimuthal directions of the beam alternately, and superimposed octupole field whose four-fold astigmatism C_{34} (radial order $R = 3$, azimuthal symmetry $S = 4$) compensates the third-order spherical aberrations C_s (C_{30} in term of R and S) in the same direction. This can be seen by observing that the XZ and YZ electron trajectories first split to form ellipses, then rejoin and are refocused at the electron gate. Fig. 8(b) illustrates the integration of such a corrector inside the resonant cavity. The system is placed in the zero-field region between the two electron mirrors (gated mirror and diffractive mirror).

Fig. 8(c) shows the raytracing simulation of the marginal and paraxial rays employing this kind of correction, both in XZ and YZ plane. This simulation demonstrates that by appropriately tuning the octupole fields C_s can be compensated. In particular, a trace stability lower than 10 nm is achieved after a full round-trip for every ray composing the beam, while in the non-compensated scheme only the marginal ray could achieve such trace stability. Therefore, we can conclude that this scheme can be efficiently used to correct spherical aberration in a linear resonant electron cavity. However, this kind of corrector is known to work in a simulation, but is extremely unstable and sensitive to misalignment, [55] which is why it took almost 50 years to go from the first theoretical proposal to an actual experimental demonstration. For this reason, in the following section, we propose an alternative scheme, easier to implement in an experimental apparatus, to correct for spherical aberration in the cavity.

3.2. Mirror corrector

Fig. 9(a) illustrates the second approach, where we substitute the gated mirror with a gate that includes a hyperbolic triode electron mirror coupled with an einzel lens on the internal side of the cavity, in place of a standard tetrode mirror. Aberration correction using a mirror in a linear electron reflector was first proposed by [32]. In this case, a modification of the beam-path design is necessary, because for the hyperbolic mirror to be effective in correcting the aberration, overlap of object and image plane in front of the mirror is required, while the previous design had a focus at the mirror surface. The hyperbolic mirror can generate negative aberrations, whose intensity depends on z_0, the position of object/image plane. z_0 is determined by the combination of the einzel lens (labeled Lens I in the figure) and the electrode below the mirror potentials (highlighted in light blue in the figure). Moreover, the value of the C_s scales as M^4 [24]. Therefore, by decreasing the focal length of the einzel lens we can increase the strength of the correction considerably. In standard triode hyperbolic mirrors, the wedge electrode potential (highlighted in yellow in the figure) represents an additional degree of freedom for tuning the correction, as it can move the position of the mirror surface. However, in our system, we have some additional constraints because the gated mirror must assure the in-coupling of the beam. Consequently, the wedge electrode potential is limited to few hundreds of volts above the 3000 V corresponding to the potential to which the electrons are accelerated, otherwise we would require too big a pulse for the in-coupling. To sustain both the reference and sample beams, this new design requires the introduction of an additional Einzel lens, labeled as Lens II in Fig. 9a. The picture illustrates in blue the reference beam and in red the sample beam axial ray.

In Fig. 9(b), simulation of the marginal and paraxial ray of the reference beam and the axial ray of the sample beam are shown. The simulated ray trajectories confirm that the resonance is achieved with this structure, and demonstrate a suppression of C_s and a trace stability below 10 nm for all the rays composing the beam. The main advantages of this design with respect to the previous one are that the sample is placed in a more accessible field-free region, in the middle of the cavity, and that the practical realization is expected to be much easier due to the lower instability and sensitivity of this kind of corrector. Conversely, since the beam is not focused but spread at the gate reflection surface (a condition necessary for the correction), the in-coupling is expected to be more difficult in terms of timing and accuracy of the beam focusing, and an additional calibrating screen will probably be required above the gated mirror. Moreover, the hyperbolic mirror corrects the aberration of one of the two beams generated by the diffractive mirror only after its first interaction with the sample, and it is reasonable to assume that this would fix the final resolution. Therefore, this approach prevents the building up of the spherical aberration induced by the diffractive mirror but it does not eliminate it completely. A ground level of aberration remains unavoidable.

4. Discussion

In this section, we discuss some of the parameters that could affect

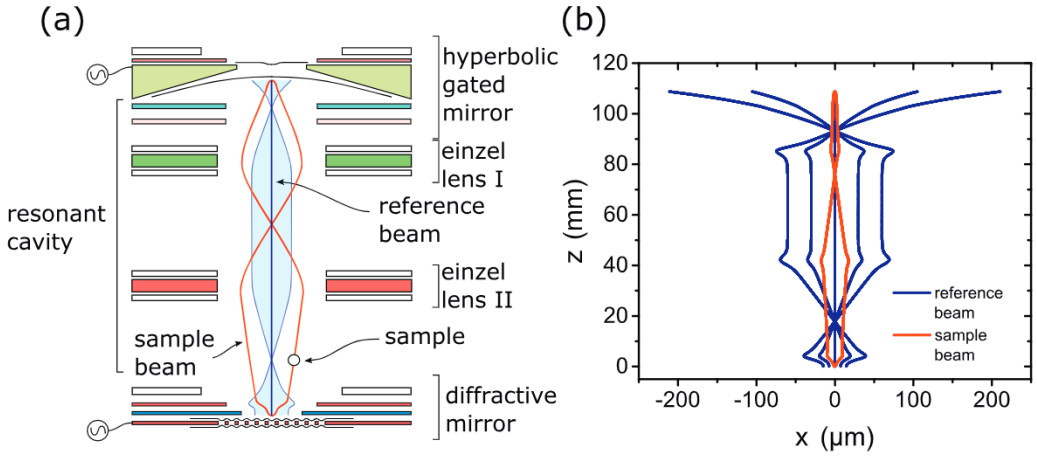

Fig. 9. (a) Diagram of the cavity corrected for spherical aberrations introducing a hyperbolic mirror in place of the standard electron gate mirror. The mirror is composed of a wedge electrode (in yellow) with slope coefficient $\sqrt{2}$ and two electrodes at distances 9.5 mm and 19 mm from it, respectively. The reference beam is shown in blue while the axial ray of the sample beam is in red. (b) Raytracing simulation portraying both the marginal and a paraxial ray in the cavity shown in (a). (For interpretation of the references to colour in this figure legend, the reader is referred to the web version of this article.)

our system such as defects and misalignment, some constraints necessary to maintain coupling, and the effect of an alignment field on the beam properties, such as the coherence of the beam. In fact, as our measurement scheme exploits interference phenomena the beam has to be coherent. In particular, we are interested in temporal coherence between the reference beam and the sample beam. Spatial coherence can be achieved by satisfying the current criterion for fully coherent beam, that is to say maintaining a beam current $I < 0.95 \cdot 10^{18} B_r$. Assuming a brightness for a typical SEM to be $B_r \sim 10^8 \frac{A}{m^2 SrV}$, we need to use a current $I < 100$ pA.

Several imperfections can occur during electron optics construction, *i.e.* machining and the assembly of electrodes, insulators, and housings. The more common defects in a round lens that can generate perturbation to the expected field are misalignment, tilt, and ellipticity [56]. In our system, the SEM optics can only correct the errors caused by the components external to the cavity. However, an additional correction unit is necessary to correct the defect generated within the resonator. In fact, as the QEM system relies on multiple reflections, the perfect control of the beam path is crucial to the success of the measurements. Misalignment or rotation can induce a phase shift, which blocks the wavefront accumulation, reduces the temporal coherence and increase the energy dispersion of the electron beam. Specifically, a cavity is extremely sensitive and even the slightest trajectory error can lead to severe consequences after few roundtrips. For instance, a 100 nm misalignment between the axis of the gated mirror and the diffractive mirror, if not corrected, causes a shift of the reference beam position on the diffractive mirror of 220 nm after just one roundtrip, which, in practice, makes any multi round-trip measurement with high resolution impossible. Therefore, it is very important for the reference beam to be located on the central axis and errors in the beam angle should be precisely corrected, as well as possible astigmatism aberration. We have also to consider that an electromagnetic alignment cannot be adopted because magnetic field force vector depends on the electron velocity direction. Therefore, an electromagnetic alignment field would generate opposite forces in the forward and reflected beam, worsening the alignment during resonance. Therefore, a double electrostatic octupole system has been chosen to fulfill these requirements [57–59]. This element exploits the superposition of quadrupole fields and azimuthally antisymmetric dipole fields to simultaneously correct astigmatism and misalignments.

Electron deflection is inversely proportional to the electron energy *E*. Therefore, an alignment field can create a parasitic chromatic spread effect, which translates in a different path length for electrons with different energies. The QEM operation relies on interference phenomena, so it is extremely important for the reference and the sample beams to maintain coherence. For this reason, it is crucial to analyze the impact of the alignment potential on the path length difference between the two, and in turn on the temporal coherence. This quantity defines the similarity between wave packets and determines the degree of interference between them. To estimate this parasitic chromatic spread effect, we can use a simple double condenser model. Using this approach, it is possible to extract the relationship between the Gaussian energy spread of the electron beam and the corresponding positional spreading in *x* direction. Hypothesizing a small deviation in the energy we can write:

$$x = \frac{K_0 V}{E \pm \sigma_E} = \frac{K_0 V}{E}\left(\frac{1}{1 \pm \sigma_E/E}\right) \sim \frac{K_0 V}{E} \mp \frac{K_0 V \sigma_E}{E^2} = x_0 \mp \sigma_x$$

Where K_0 is a geometrical constant, E is the central energy, V is the deflection potential and σ_E and σ_x are the standard deviations of energy and position respectively. Once the E is fixed, we can conclude that $\sigma_x = K_1 V \sigma_E$; where $K_1 = K_0/E^2$ is a constant dependent on the geometry and the central energy. The electron optical simulation of our deflection system confirmed the validity of this model and, hypothesizing a Gaussian distribution centered at 3 keV, we extracted the corresponding constant $K_1 = 5 \cdot 10^{-11}$m/(V · eV). Fig. 10(a) is a graphical representation of this chromatic aberration phenomenon. It shows the distribution of the electron density of an electron beam after passing through the aligner as a function of the misalignment. The electron beam is initially confined to a single trajectory but with $\Delta E \sim 2\sigma_E = 0.7$ eV. The resulting spread is an important parameter to characterize the correct functioning of the system. At each round trip, this phenomenon will worsen the resolution by increasing the beam size due to chromatic aberration d_c. Therefore, the alignment precision during manufacturing should be specified keeping in mind this effect that plays an important role in the final resolution.

In order to analyze the impact of the alignment potential on the temporal coherence, it is possible to define the temporal coherence length [5] $\lambda_C = vh/\Delta E$, where v is the electron velocity and h is the Planck constant. In our case, $\lambda_C \sim 150$ nm. When an alignment field is applied, the beam deflection is not rigid, as in an ideal case, but it occurs throughout a finite region. Due to the angle between reference and sample beams, these beams experience different deflection lengths. In particular, the beam whose bending is along the direction of the alignment has a higher deflection length than the one that is aligned against the deflection field. This results in a positive and negative path length difference with respect to the reference beam path, respectively. Fig. 10(b) shows the outcome of the simulation of this path length

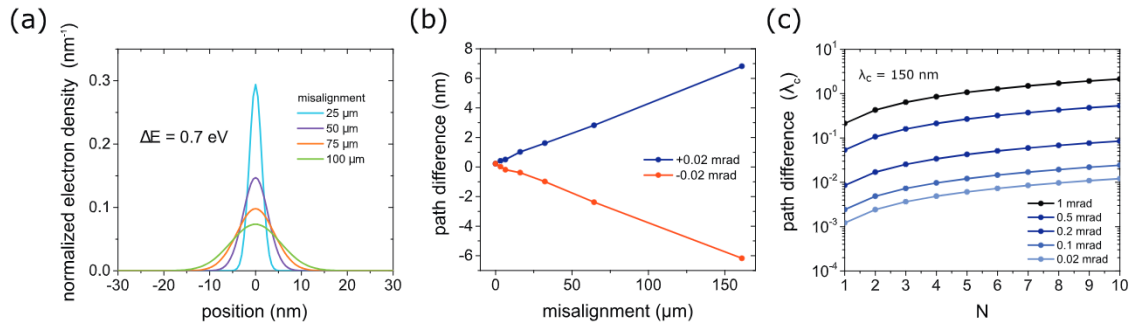

Fig. 10. (a) Graph showing the position spread of an electron beam in terms of its normalized electron density while varying the alignment potential. The electrons composing the initial beam are localized in one trajectory, but they have $\Delta E = 0.7$ eV energy spread. This lead to a spatial spread after passing through the aligner, that depends on the alignment strength with the relationship: $\sigma_x = 5{\cdot}10^{-11}{\cdot}V{\cdot}\sigma_E$. (b) Simulation of the path difference between the two branches of the sample beam and the reference beam due to the influence of the alignment field. This effect has to be considered in the calculation of the mechanical precision required to maintain temporal coherence. Luckily the effect is compensated every two roundtrips so it does not worsen with the number of roundtrips. However, its magnitude increases with the angle between reference and sample beam. (c) Path difference between the sample and the reference beams with the number of roundtrips for different angles. The path difference is expressed in unit of temporal coherence length λ_C.

difference for different alignment potentials, expressed in terms of the correspondent misalignments that they correct. This simulation is performed for a 0.02 mrad angle between reference and sample beams, correspondent to a 1 μm periodicity of the grating and an electron wavelength of $\lambda_E = 22$ pm ($E = 3$ keV), but the effect becomes more important for larger angles. This path difference must be added to the unavoidable component coming from the fact that reference beam and sample beams have different directions, but they experience reflection at the electron gate on the same Gaussian plane. Therefore, they have an intrinsic geometrical path length difference, positive for both diffracted beams ($m = \pm 1$) which we simulated, and is illustrated in Fig. 10(c). In this picture, this path difference is shown for different diffraction angles (different grating periodicities) while increasing N. Both these components, the one due to the alignment and the one due to the diffraction angle, add to the total path length difference between the sample and the reference beams. Fortunately, the progression of the path difference is linear with N and depends only on the angle, regardless of the alignment because the alignment component compensate every two roundtrips (it causes an alternation of positive and negative path difference). Therefore, the alignment component should be taken into account but does not build up with N. In Fig. 10(c) the vertical axis is scaled in λ_C units so the region of operation is limited to the semi-plane below unity, which determines the maximum useful θ and N. To determine a similar region in terms of maximum misalignment we have to take into account also the component due to the alignment potential. If we consider an angle of 0.02 mrad, for $N = 10$ we obtain a path difference of the order of 10 nm which is $< \lambda_C \sim 150$ nm, so temporal coherence is preserved in the system.

Quantum electron microscopy requires the electron beams to interact with a phase grating multiple times and thus accumulate the wavefront modulation, as graphically illustrated in Fig. 11. This requires a good alignment between the grating and the modulated electron beam wavefront. A misalignment between the grating and the wavefront will cause a phase error, which blocks the accumulation of wavefront modulation. For example, consider a QEM with $N = 13$. The misalignment reduces the magnitude of intensity transfer between the sample beam and the reference beam, thus compromising the accuracy of QEM in differentiating a white pixel and a black pixel. Fig. 12 shows such a degradation of the intensity of the reference and the sample beams for different values of the phase error.

A particularly important issue of this apparatus that has to be addressed in the future is the complexity of the diagnostics due to the resonant nature of the system, which does not allow access to the beam in the cavity. This problem is particularly significant for the aberration correction where an assessment of the performance after the correction would be ideal to modify the free parameters accordingly. This fact calls

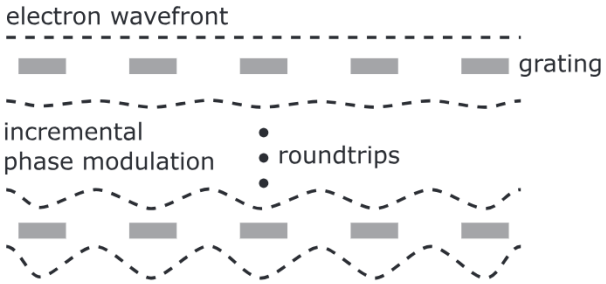

Fig. 11. Graphical illustration of the electron wavefunction incremental modulation passing through a phase grating multiple times. In our system, the electron beam is reflected at the grating but the concept is equivalent to a transmission grating.

for the definition of a diagnostic protocol, the necessity of an extremely precise and reliable modeling of the system and strong machining and alignment requirements.

5. Conclusion

In conclusion, it is possible to design a resonant electron cavity for a QEM-in-SEM system employing ray-tracing methods to verify the beam characteristics with the progression of the round-trips. Such a design satisfies the practical design constraints and is able to maintain the system stability and the coherence between the reference and sample beams. It is also possible to compensate for the third-order spherical aberrations inside the cavity using a hyperbolic mirror or a quadrupole-octupole corrector, and to correct machining and assembly misalignments by introducing an alignment unit. The realization of such a resonant cavity would allow the proof-of-concept demonstration of a system able to significantly reduce the radiation damage adopting an interaction-free measurement scheme into an SEM. This work is part of the ongoing effort for achieving direct imaging of macromolecules with sub-nm resolution. Future work will include the experimental demonstration of the elements composing the cavity and of their integration to build the complete system, as well as additional effort in improving the performance of the cavity in terms of imaging resolution.

Acknowledgements

This work was supported by Gordon and Betty Moore Foundation. We would also like to acknowledge the Chu Family Foundation for support. Finally, we thank the GBMF QEM teams at MIT, Stanford University, University of Erlangen, and the Delft University of

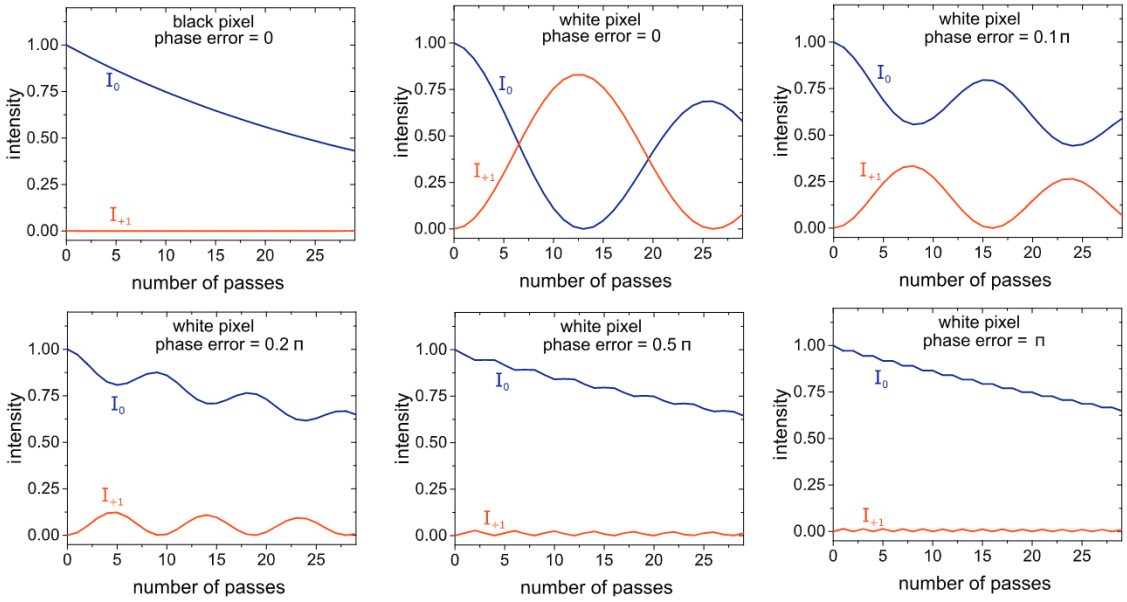

Fig. 12. Intensity of the reference (I_0) and sample (I_{+1}) beams as a function of the number of roundtrip in case of a black pixel or a white pixel for different values of phase error on the diffractive mirror. Comparing the top left figure with each of the others we can clearly see that when the phase error increases, the black and white pixels become no longer distinguishable.

Technology for many helpful technical discussions. In particular, we thank the Stanford team and Marian Mankos for pointing out to us the possibility of adopting the gated mirror to also serve as an aberration corrector, and Maurice Krielaart from the Delft team for sharing with us his early results on the diffraction mirror simulation.

References

[1] R. Henderson, The potential and limitations of neutrons, electrons and x-rays for atomic resolution microscopy of unstained biological molecules, Q. Rev. Biophys. 28 (1995) 171, https://doi.org/10.1017/S003358350000305X.
[2] R.M. Glaeser, Limitations to significant information in biological electron microscopy as a result of radiation damages, J. Ultrastruct. Res. 36 (1971) 466–482, https://doi.org/10.1016/S0022-5320(71)80118-1.
[3] R.M. Glaeser, K.A. Taylor, Radiation damage relative to transmission electron microscopy of biological specimens at low temperature: a review, J. Microsc. 112 (1978) 127–138, https://doi.org/10.1111/j.1365-2818.1978.tb01160.x.
[4] R.F. Egerton, P. Li, M. Malac, Radiation damage in the TEM and SEM, Micron. 35 (2004) 399–409, https://doi.org/10.1016/j.micron.2004.02.003.
[5] D.B. Williams, C.B. Carter, Transmission Electron Microscopy: A Textbook for Materials Science, Springer, 2009, https://doi.org/10.1007/978-0-387-76501-3.
[6] C.A. Diebolder, A.J. Koster, R.I. Koning, Pushing the resolution limits in cryo electron tomography of biological structures, J. Microsc. 248 (2012) 1–5, https://doi.org/10.1111/j.1365-2818.2012.03627.x.
[7] W. Kulbrandt, Microscopy: Cryo-EM enters a new era, elife 3:e03665, (2014), doi:10.7554/eLife.03678.
[8] S.H.W. Scheres, R. Nunez-Ramirez, C.O.S. Sorzano, J.M. Carazo, R. Marabini, Image processing for electron microscopy single-particle analysis using XMIPP, Nat. Protoc. 3 (2008) 977–990, https://doi.org/10.1038/nprot.2008.62.
[9] R.M. Glaeser, How good can cryo-EM become? Nat. Methods. 13 (2016) 28–32, https://doi.org/10.1038/nmeth.3695.
[10] P.T. Ho, V.S. Reddy, Rapid increase of near atomic resolution virus capsid structures determined by cryo-electron microscopy, J. Struct. Biol. 201 (2017) 1–4, https://doi.org/10.1016/j.jsb.2017.10.007.
[11] E. Callaway, The revolution will not be crystallized: a new method sweeps through structural biology, Nature 525 (2015) 172–174, https://doi.org/10.1038/525172a.
[12] S.J. Ludtke, P.R. Baldwin, W. Chiu, EMAN: semiautomated software for high-resolution single-particle reconstructions, J. Struct. Biol. 128 (1999) 82–97, https://doi.org/10.1006/jsbi.1999.4174.
[13] H. Okamoto, T. Latychevskaia, H.W. Fink, A quantum mechanical scheme to reduce radiation damage in electron microscopy, Appl. Phys. Lett. 88 (2006), https://doi.org/10.1063/1.2191096.
[14] H. Okamoto, Y. Nagatani, Entanglement-assisted electron microscopy based on a flux qubit, Appl. Phys. Lett. 104 (2014), https://doi.org/10.1063/1.4865244.
[15] H.W. Fink, W. Stocker, H. Schmid, Holography with low-energy electrons, Phys. Rev. Lett. 65 (1990) 1204–1206, https://doi.org/10.1103/PhysRevLett.65.1204.
[16] M.J. Humphry, B. Kraus, A.C. Hurst, A.M. Maiden, J.M. Rodenburg, Ptychographic electron microscopy using high-angle dark-field scattering for sub-nanometre resolution imaging, Nat. Commun. 3 (2012), https://doi.org/10.1038/ncomms1733.
[17] T. Juffmann, S.A. Koppell, B.B. Klopfer, C. Ophus, R.M. Glaeser, M.A. Kasevich, Multi-pass transmission electron microscopy, Sci. Rep. 7 (2017) 1–7, https://doi.org/10.1038/s41598-017-01841-x.
[18] P. Kruit, R.G. Hobbs, C.S. Kim, Y. Yang, V.R. Manfrinato, J. Hammer, S. Thomas, P. Weber, B.B. Klopfer, C. Kohstall, T. Juffmann, M.A. Kasevich, P. Hommelhoff, K.K. Berggren, Designs for a quantum electron microscope, Ultramicroscopy. 164 (2016) 31–45, https://doi.org/10.1016/j.ultramic.2016.03.004.
[19] W.P. Putnam, M.F. Yanik, Noninvasive electron microscopy with interaction-free quantum measurements, Phys. Rev. A. 80 (2009), https://doi.org/10.1103/PhysRevA.80.040902.
[20] M. Larsson, Atomic and molecular physics with ion storage rings, Reports Prog. Phys. 58 (1995) 1267–1319, https://doi.org/10.1088/0034-4885/58/10/003.
[21] J. Bernard, G. Montagne, R. Brédy, B. Terpend-Ordacière, A. Bourgey, M. Kerleroux, L. Chen, H.T. Schmidt, H. Cederquist, S. Martin, A “tabletop” electrostatic ion storage ring: mini-ring, Rev. Sci. Instrum. 79 (75109) (2008). 10.1063/1.2957609
[22] G.R. Rempfer, A theoretical study of the hyperbolic electron mirror as a correcting element for spherical and chromatic aberration in electron optics, J. Appl. Phys. 67 (1990), https://doi.org/10.1063/1.345212.
[23] J.P.S. Fitzgerald, R.C. Word, R. Konenkamp, Adaptive aberration correction using a triode hyperbolic electron mirror, Ultramicroscopy 111 (2011) 1495–1503, https://doi.org/10.1016/j.ultramic.2011.06.004.
[24] J.P.S. Fitzgerald, R.C. Word, R. Konenkamp, Simultaneous and independent adaptive correction of spherical and chromatic aberration using an electron mirror and lens combination, Ultramicroscopy. 115 (2012) 35–40, https://doi.org/10.1016/j.ultramic.2012.02.001.
[25] P. Hommelhoff, C. Kealhofer, M.A. Kasevich, Ultrafast electron pulses from a tungsten tip triggered by low-power femtosecond laser pulses, Phys. Rev. Lett. 97 (247402) (2006), https://doi.org/10.1103/PhysRevLett.97.247402.
[26] D. Ehberger, J. Hammer, M. Eisele, M. Krger, J. Noe, A. Hgele, P. Hommelhoff, Highly coherent electron beam from a laser-triggered tungsten needle tip, Phys. Rev. Lett. 114 (2015), https://doi.org/10.1103/PhysRevLett.114.227601. 227601
[27] A. Feist, N. Bach, N.R.d. Silva, T. Danz, M. Mller, K.E. Priebe, T. Domrse, J.G. Gatzmann, S. Rost, J. Schauss, S. Strauch, R. Bormann, M. Sivis, S. Schfer, C. Ropers, Ultrafast transmission electron microscopy using a laser-driven field emitter: femtosecond resolution with a high coherence electron beam, Ultramicroscopy 176 (2017) 63–73, https://doi.org/10.1016/j.ultramic.2016.12.005.
[28] F. Houdellier, G.M. Caruso, S. Weber, M. Kociak, A. Arbouet, Development of a high brightness ultrafast transmission electron microscope based on a laser-driven cold field emission source, Ultramicroscopy 186 (2018) 128–138, https://doi.org/10.1016/j.ultramic.2017.12.015.
[29] R.J. Moerland, I.G.C. Weppelman, M.W.H. Garming, P. Kruit, J.P. Hoogenboom, Time-resolved cathodoluminescence microscopy with sub-nanosecond beam blanking for direct evaluation of the local density of states, Opt. Express 24 (21) (2016) 24760–24772, https://doi.org/10.1364/OE.24.024760.
[30] I.G.C. Weppelman, R.J. Moerland, J.P. Hoogenboom, P. Kruit, Concept and design of a beam blanker with integrated photoconductive switch for ultrafast electron microscopy, Ultramicroscopy 184 B (2018) 8–17, https://doi.org/10.1016/j.ultramic.2017.10.002.
[31] S. Meuret, M.S. Garcia, T. Coenena, E. Kieft, H. Zeijlemaker, M. Ltzel, S. Christiansen, S.Y. Woo, Y.H. Ra, Z. Mi, A. Polman, Complementary cathodoluminescence lifetime imaging configurations in a scanning electron

microscope, Ultramicroscopy 197 (2019) 28–38, https://doi.org/10.1016/j.ultramic.2018.11.006.
[32] US patent 7902504b2, charged particle beam reflector device and electron microscope, Topcon KK, 2007. https://patents.google.com/patent/US7902504.
[33] A.U. MacRae, Low-energy electron diffraction, Science (80-.) 139 (1963) 379–388, https://doi.org/10.1126/science.139.3553.379.
[34] H. Lichte, M. Lehmann, Electron holography - basics and applications, Reports Prog. Phys. 71 (2008), https://doi.org/10.1088/0034-4885/71/1/016102.
[35] Y. Yang, C.S. Kim, R.G. Hobbs, P. Kruit, K.K. Berggren, Efficient two-port electron beam splitter via a quantum interaction-free measurement, Phys. Rev. A 98 (2018), https://doi.org/10.1103/PhysRevA.98.043621.
[36] S. Thomas, C. Kohstall, P. Kruit, P. Hommelhoff, Semitransparency in interaction-free measurements, Phys. Rev. A 90 (2014) 053840, https://doi.org/10.1103/PhysRevA.90.053840.
[37] A. Elitzur, L. Vaidman, Quantum mechanical interaction-free measurements, Found. Phys. 23 (1995) 987, https://doi.org/10.1007/BF00736012.
[38] P. Kwiat, H. Weinfurter, T. Herzog, A. Zeilinger, M.A. Kasevich, Interaction-free measurement, Phys. Rev. Lett. 74 (1995) 4763, https://doi.org/10.1103/PhysRevLett.74.4763.
[39] B. McMorran, J.D. Perreault, T.A. Savas, A. Cronina, Diffraction of 0.5 keV electrons from free-standing transmission gratings, Ultramicroscopy 106 (2006) 356, https://doi.org/10.1016/j.ultramic.2005.11.003.
[40] T. Leuthner, H. Lichte, K.H. Herrmann, STEM-Holography using the electron biprism, Phys. Stat. Sol. 116 (1989) 113, https://doi.org/10.1002/pssa.2211160111.
[41] M.A.R. Krielaart, P. Kruit, Grating mirror for diffraction of electrons, Phys. Rev. A 98 (2018) 063806, https://doi.org/10.1103/PhysRevA.98.063806.
[42] H. Rose, Geometrical charged-Particle optics, Springer, 2009, https://doi.org/10.1007/978-3-540-85916-1.
[43] M. Lenc, I. Mullerova, Electron optical properties of a cathode lens, Ultramicroscopy 41 (1992) 411–417, https://doi.org/10.1016/0304-3991(92)90220-E.
[44] M. Lenc, I. Mullerova, Measuring and correcting aberrations of a cathode objective lens, Ultramicroscopy 111 (2011) 273–281, https://doi.org/10.1016/j.ultramic.2010.11.029.
[45] R.M. Tromp, W. Wanb, S.M. Schramm, Aberrations of the cathode objective lens up to fifth order, Ultramicroscopy 119 (2012) 33–39, https://doi.org/10.1016/j.ultramic.2011.09.011.
[46] E. Bauer, Low energy electron microscopy, Reports Prog. Phys. 57 (895) (1994), https://doi.org/10.1088/0034-4885/57/9/002.
[47] P. Hartel, D. Preikszas, R. Spehr, H. Müller, H. Rose, Mirror corrector for low-voltage electron microscopes, Adv. Imaging Electron Phys. 120 (2003) 41–133, https://doi.org/10.1016/S1076-5670(02)80034-9.
[48] R.H.V. Aken, D.J. Maas, C.W. Hagen, J.E. Barth, P. Kruit, Design of an aberration corrected low-voltage SEM, Ultramicroscopy 110 (2010) 1411–1419, https://doi.org/10.1016/j.ultramic.2010.07.012.
[49] O. Scherzer, Uber einige fehler von elektronenlinsen, Zeitschrift Für Phys. 101 (1936) 593–603, https://doi.org/10.1007/BF01349606.
[50] P.E. Batson, N. Dellby, O.L. Krivanek, Sub-angstrom resolution using aberration corrected electron optics, Nature 418 (2002) 617–620, https://doi.org/10.1038/nature00972.
[51] O.L. Krivanek, N. Dellby, A.R. Lupini, Towards sub-a electron beams, Ultramicroscopy. 78 (1999) 1–11, https://doi.org/10.1016/S0304-3991(99)00013-3.
[52] G. Schonhense, H. Spiecker, Correction of chromatic and spherical aberration in electron microscopy utilizing the time structure of pulsed excitation sources, J. Vac. Sci. Technol. B. 20 (2002) 2526–2534, https://doi.org/10.1116/1.1523373.
[53] R.H.V. Aken, C.W. Hagen, J.E. Barth, P. Kruit, Low-energy foil aberration corrector, Ultramicroscopy. 93 (2002) 321–330, https://doi.org/10.1016/S0304-3991(02)00287-5.
[54] G.D. Archard, Two new simplified systems for the correction of spherical aberration in electron lenses, Proc. Phys. Soc. B. 68 (1954) 778, https://doi.org/10.1088/0370-1301/68/3/305.
[55] P.W. Hawkes, Aberration correction past and present, Philos. Trans. R. Soc. A Math. Phys. Eng. Sci. 367 (2009) 3637–3664, https://doi.org/10.1098/rsta.2009.0004.
[56] E. Munro, Finite difference programs for computing tolerances for electrostatic lenses, J. Vac. Sci. Technol. B. 6 (1988) 941, https://doi.org/10.1116/1.584329.
[57] W.P. Li, L. Han, W.Q. Gu, Design of practical deflection field in nanometer-scale focused ion beam system, Nucl. Instrum. Methods Phys. Res. A. 579 (2007) 937–940, https://doi.org/10.1016/j.nima.2007.06.012.
[58] K. Kanaya, H. Kawakatzu, Deflection system with eight-pole stigmator used in correcting astigmatism, J. Electron Microsc. (Tokyo) 10 (1961) 281, https://doi.org/10.1093/oxfordjournals.jmicro.a049311.
[59] M. Szilagyi, Electron and ion optics, Plenum Press, 1988, https://doi.org/10.1007/978-1-4613-0923-9.